ACS OMEGA

http://pubs.acs.org/journal/acsodf

Article

Battery-Type-Behavior-Retention $Ni(OH)_2$–rGO Composite for an Ultrahigh-Specific-Capacity Asymmetric Electrochemical Capacitor Electrode

Binglin Guo, Yihao Gao, Yongyue Li, Kai Liu, Xiaojun Lv, Changhua Mi, Lehao Liu, and Meicheng Li*

Cite This: *ACS Omega* 2023, 8, 6289–6301

Read Online

ACCESS | Metrics & More | Article Recommendations | Supporting Information

ABSTRACT: Nanosized battery-type materials applied in electrochemical capacitors can effectively reduce a series of problems caused by low conductivity and large volume changes. However, this approach will lead to the charging and discharging process being dominated by capacitive behavior, resulting in a serious decline in the specific capacity of the material. By controlling the material particles to an appropriate size and a suitable number of nanosheet layers, the battery-type behavior can be retained to maintain a large capacity. Here, $Ni(OH)_2$, which is a typical battery-type material, is grown on the surface of reduced graphene oxide to prepare a composite electrode. By controlling the dosage of the nickel source, the composite material with an appropriate $Ni(OH)_2$ nanosheet size and a suitable number of layers was prepared. The high-capacity electrode material was obtained by retaining the battery-type behavior. The prepared electrode had a specific capacity of 397.22 mA h g^{-1} at 2 A g^{-1}. After the current density was increased to 20 A g^{-1}, the retention rate was as high as 84%. The prepared asymmetric electrochemical capacitor had an energy density of 30.91 W h kg^{-1} at a power density of 1319.86 W kg^{-1} and the retention rate could reach 79% after 20,000 cycles. We advocate an optimization strategy that retains the battery-type behavior of electrode materials by increasing the size of nanosheets and the number of layers, which can significantly improve the energy density while combining the advantage of the high rate capability of the electrochemical capacitor.

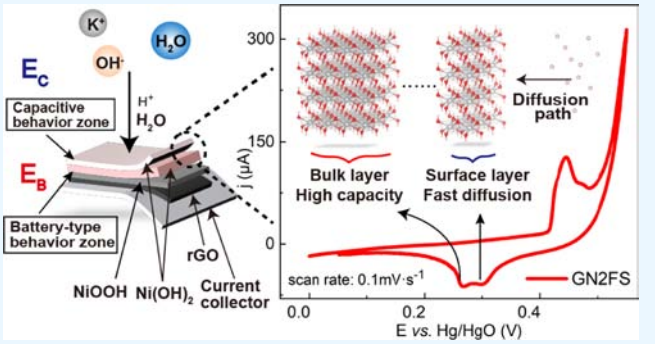

INTRODUCTION

Renewable energy is usually distributed unevenly in time and space, which requires energy storage devices for energy supply on demand. Batteries and electrochemical capacitors are typical advanced energy storage devices.[1] Energy storage devices represented by lithium-ion batteries and sodium-ion batteries have an excellent energy density, which can reach about 250 W h kg^{-1}.[2] At the same time, they have a mature and stable production process and have achieved mass production.[3] However, the power density and cycle performance of these devices are insufficient, which leads to limited application.[4] Electrochemical capacitors have outstanding and satisfying power density, cycle performance, and charge–discharge efficiency. In some scenarios, such as electric vehicles and power grid peaking, they have the potential to replace the batteries for energy storage.[5,6] Currently, a concern to be solved in electrochemical capacitors is the relatively low energy density, especially compared with lithium-ion or sodium-ion batteries. Therefore, a large number of studies are involved in improving the energy density of electrochemical capacitors, and the selection of electrode materials greatly affects the electrochemical performance of devices.[7]

According to the mechanism of energy storage, the existing electrode materials can be grouped into three types: electric double-layer materials, pseudocapacitive materials, and battery-type materials. An electric double-layer material mainly relies on the electrostatic adsorption of electrolyte ions on the electrode surface to store energy, which is a physical process. Therefore, electric double-layer materials have long cycle life and high energy efficiency, but their capacity needs to be improved. Common materials include porous carbon[8] and graphene.[9,10] Both pseudocapacitive materials and battery-type materials store energy by redox reactions. The main difference is that the battery-type materials are controlled by diffusion during the electrochemical process, while the capacitive materials are controlled by the surface process. Typical pseudocapacitive materials mainly include RuO_2,[11,12] MnO_2,[13,14] and Fe_2O_3.[15,16] During the electrochemical process,

Received: September 26, 2022
Accepted: December 15, 2022
Published: February 13, 2023

the redox reaction mainly occurs on the surface of the material or near the electrode/electrolyte interface, which belongs to a surface control process.[17] Intercalation pseudocapacitance materials store energy by capacitive behavior, both bulk and nanosized, with highly reversible and fast reaction kinetics.[18] Battery-type materials which generally have a considerable specific capacity are controlled by diffusion during the electrochemical process. For example, $LiCoO_2$ shows typical battery behavior in a bulk state. When the particle size of $LiCoO_2$ is reduced below a certain value, it will show capacitance-like behavior, and such materials are defined as extrinsic pseudocapacitance materials.[19]

An asymmetric electrochemical capacitor (AEC) based on battery-type cathode materials retains the advantages of electrochemical capacitors, while their energy density also can be improved by the advantage of the large capacity of battery-type materials.[20,21] With high theoretical capacity, low cost, environmental friendliness, and stable properties in alkaline electrolytes, $Ni(OH)_2$ can be seen as a promising battery-type material. However, low intrinsic conductivity, large volume change, and easy degradation and falling off lead to unsatisfactory rate capability and cycle stability of $Ni(OH)_2$, which seriously limit its application in electrochemical energy storage.[22,23] With the development of nanomaterials, a considerable number of studies have been carried out to reduce $Ni(OH)_2$ particles to the nanoscale. To achieve the preparation of low-internal-resistance and high-efficiency electrode materials by shortening the electron and ion transmission distance, the electrode/electrolyte interface area and exposed active sites were increased after nanocrystallization. A hierarchical CoS_2@$Ni(OH)_2$ core−shell nanotube array was prepared by Luo et al. The CoS_2 nanotube structure served as a kind of scaffold with a 50 nm ultrathin $Ni(OH)_2$ sheet grown on the surface. The uniform distribution could improve the interfacial contact between the electrode and electrolyte and facilitate ion and electron transfer. The assembled supercapacitor provides a capacity of 743 C g^{-1} at 1 A g^{-1}.[24] Li et al. prepared a corrugated β-$Ni(OH)_2$ with a thickness of about 10 nm which provides abundant electroactive sites and improves the rate capability and cycling performance, featuring a capacity of 457 C g^{-1} at 30 A g^{-1} and maintaining 91% capacity after 10,000 cycles.[25] Li et al. prepared an α-$Ni(OH)_2$ nanowire material with a three-dimensional mesh structure containing SO_4^{2-} with a diameter of about 20 nm. The surface structure was able to guarantee the existence of a sufficient interface between the electrode and electrolyte, which made the electrode present a capacity of 246.3 mA h g^{-1} at 1 A g^{-1} and 91.7% retention after 4000 cycles.[26]

Obviously, nanoscale electrode materials can be an effective way to solve large internal resistance and easy degradation and falling off of materials during cycling. However, there is enough evidence for battery-type materials that the specific capacity will decline in quantity when the material particle is reduced below a certain size.[27−29] For example, Okubo et al. pointed out that when the particle size of $LiCoO_2$ was reduced from 17 to 6 nm, the number of layers decreased and the surface layers took more parts, leading to a significant increase in the proportion of capacitive behavior of the electrode and a measurable decrease in the specific capacity of the electrode. This phenomenon related to the number of layers is called the surface layer effect, indicating that there is a great correlation between the specific capacity of the electrode and the particle size.[30] Although higher rate capability and cycle performance can be obtained, excessive nanocrystallization electrode materials can hardly achieve high capacity. Therefore, when preparing $Ni(OH)_2$ nanosheets, through the control of production conditions, nanosheets with a certain size and thickness are obtained to have the battery-type behavior retained (as illustrated in Scheme 1). This is expected to prepare electrodes combined with large capacity, high-rate capability, and long cycle life all in one.

Scheme 1. Schematic Illustration of the $Ni(OH)_2$−rGO Composite in the Discharging Process

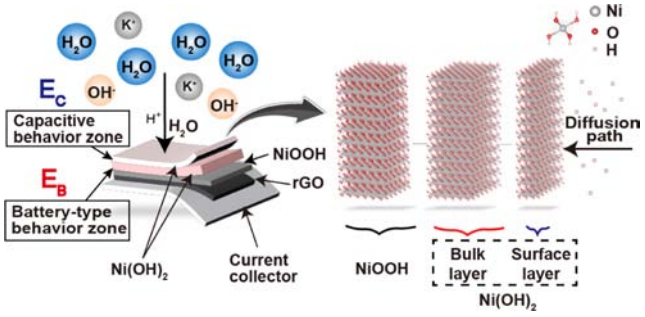

Herein, $Ni(OH)_2$ was grown in situ on the surface of reduced graphene oxide (rGO) by a simple hydrothermal method. The prepared electrode has a specific capacity of 397.22 mA h g^{-1} at a current density of 2 A g^{-1}. The retention rate is as high as 84% when increasing the current density to 20 A g^{-1}. The AEC is prepared with the mentioned composite materials and activated carbon (AC) as the positive and negative electrodes, respectively. At 1319.86 W kg^{-1}, the energy density is 30.91 W h kg^{-1}, and the retention rate is 79% after 20,000 charging and discharging cycles. The micromorphology of $Ni(OH)_2$ nanosheets was controlled by changing the Ni source dosage. $Ni(OH)_2$ nanosheets with relatively large particle sizes of about 50 nm and more than 30 layers were obtained. This appropriate size and the suitable number of nanosheet layers can retain the battery-type behavior in the electrochemical process to achieve a large specific capacity.

Meanwhile, using rGO as the substrate can effectively alleviate a series of problems caused by the larger nanosheet size and realize the retention of fast reaction kinetics. GO was treated and reduced to rGO under alkaline conditions and had better conductivity. The oxygen-containing functional groups (OFGs) on the surface of GO can guide the in situ growth of $Ni(OH)_2$ nanosheets to obtain a moss-like morphology during the hydrothermal process. As a highly conductive carbon substrate, rGO rapidly exports electrons to achieve a high rate capability. The degradation and falling off of $Ni(OH)_2$ nanosheets were ameliorated by the protection of high mechanical-strength rGO, and the cycle life of the electrode was extended.

RESULTS AND DISCUSSION

$Ni(OH)_2$−rGO composites were prepared by the hydrothermal method. By changing the dosage of $NiSO_4{\cdot}6H_2O$ and NaOH, the mass ratios of GO and $Ni(OH)_2$ were 1:1, 1:2, 1:5, and 1:10, named as GN1, GN2, GN5, and GN10, respectively. The morphology and microstructure of GN1, GN2, and GN5 are shown in Figure 1. For GN1, the high-magnification

https://doi.org/10.1021/acsomega.2c06207
ACS Omega 2023, 8, 6289−6301

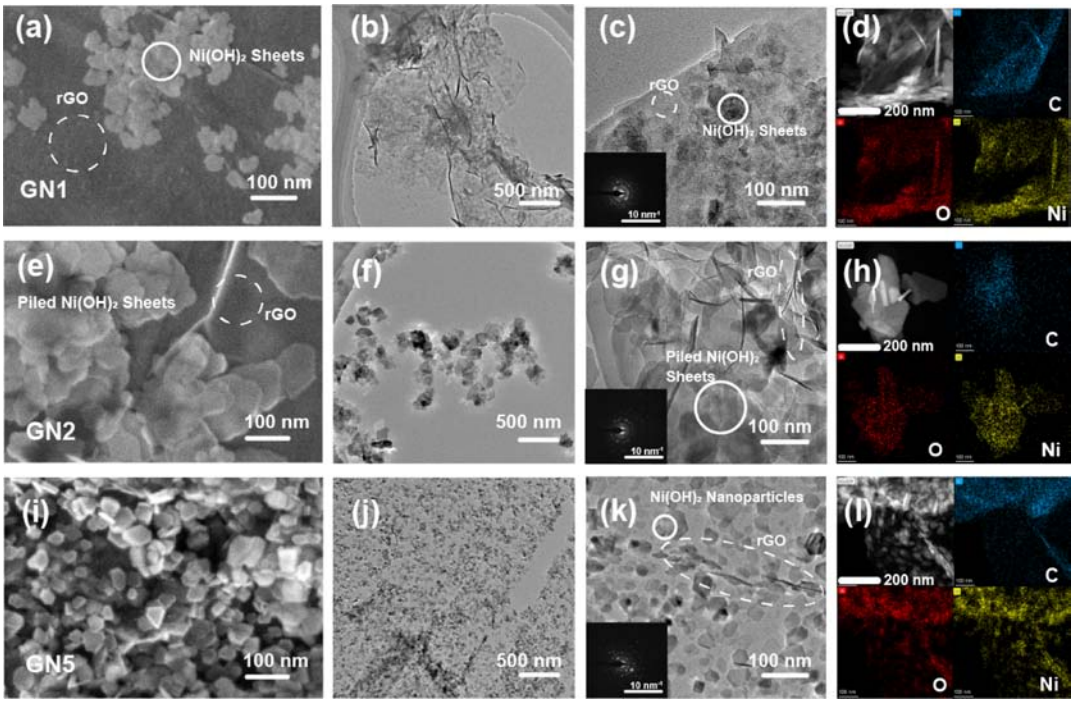

Figure 1. SEM images of (a) GN1, (e) GN2, and (i) GN5 at different magnifications. TEM images of (b,c) GN1, (f,g) GN2, and (j,k) GN5; inset images are the SAED patterns. Mapping images of (d) GN1, (h) GN2, and (l) GN5.

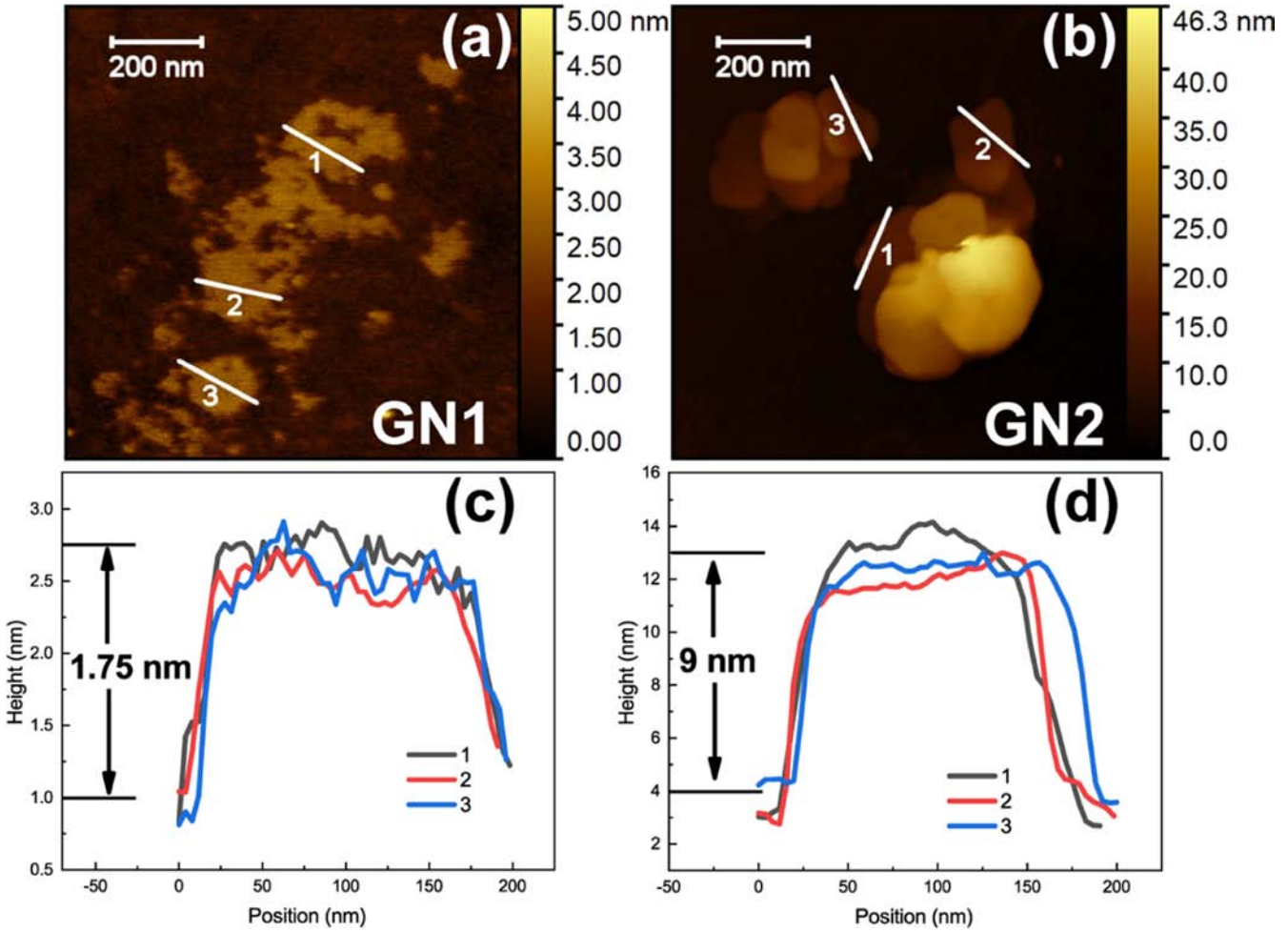

Figure 2. AFM micrographs of (a) GN1 and (b) GN2 and the height profiles of (c) GN1 and (d) GN2.

https://doi.org/10.1021/acsomega.2c06207
ACS Omega 2023, 8, 6289−6301

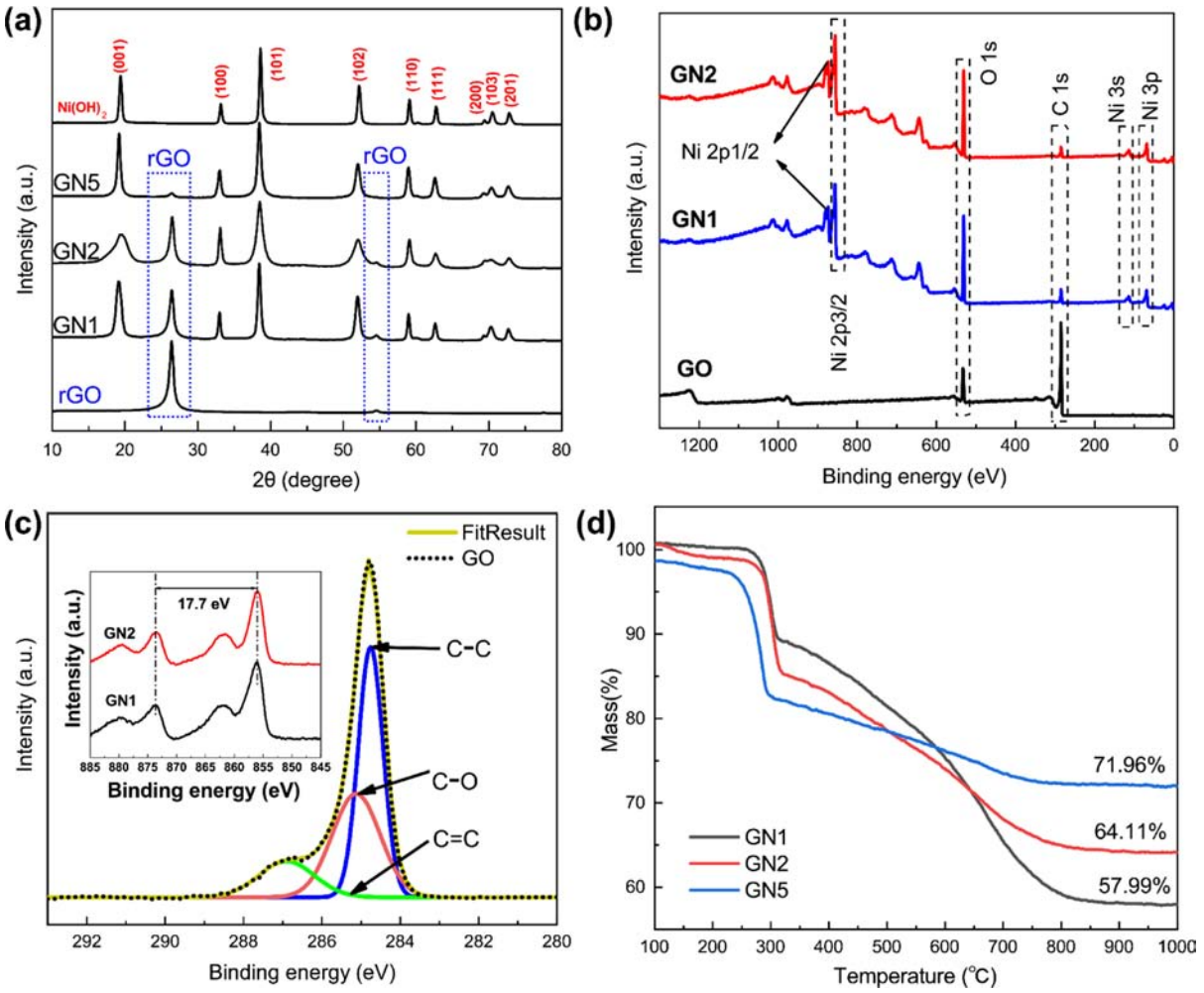

Figure 3. (a) XRD patterns of GN1, GN2, GN5, rGO, and $Ni(OH)_2$. (b) Survey scan of XPS spectra of GO, GN1, and GN2. (c) C 1s spectra and Ni 2p spectra (inset). (d) TGA curves of composite materials.

scanning electron microscopy (SEM) images are shown in Figure 1a and the transmission electron microscopy (TEM) images are shown in Figure 1b,c. The mapping image of GN1 is shown in Figure 1d. Due to the low dosage of NaOH and $NiSO_4{\cdot}6H_2O$, only a fraction of $Ni(OH)_2$ nanosheets which are thin and boundary-fuzzy grow on the surface of rGO. Due to the small thickness, $Ni(OH)_2$ nanosheets are difficult to distinguish, as shown in Figure 1b. The SEM and TEM images of GN2 can be seen in Figure 1e−g. Figure 1h shows the mapping image of GN2. The moss-like $Ni(OH)_2$ nanosheets are stacked obviously and are significantly thicker than those of GN1, while their size is about 50 nm; the nanosheet size distributions of GN2 and GN5 are shown in Figure S1. The edge of $Ni(OH)_2$ nanosheets is clear and grown along the surface of rGO. The interplanar distance of GN2 is 0.27 nm, corresponding to the (100) crystal plane of β-$Ni(OH)_2$ as shown in Figure S2.[31] Supplementary SEM images of GN1, GN2, and GN5 can be seen in Figure S3. With the increase of the nickel source dosage, a large number of $Ni(OH)_2$ nanohexagonal prisms are grown in the hydrothermal process rather than grown in situ on the surface of rGO after being adsorbed by the OFG. Therefore, the formed short hexagonal prisms of GN5, which are shown in Figure 1i, are different from the flat moss-like morphology of GN2. The size of the nanohexagonal prisms on the surface of GN5 as shown in Figure 1j is much smaller than that of GN2. The rGO wrinkle can be seen clearly in Figure 1k. Figure 1l is the mapping image of GN5, and the $Ni(OH)_2$ nanohexagonal prisms can be easily differentiated. For GN10 synthesized with a high dosage of NaOH and $NiSO_4{\cdot}6H_2O$, it is difficult to find rGO in Figure S4a. $Ni(OH)_2$ particles in the high-magnification image are hexagonal with some broken particles, which are shown in Figure S4b. The particle size is about 100 nm, larger than that of GN5.

The atomic force microscopy (AFM) micrographs were used to calculate the thickness of $Ni(OH)_2$ nanosheets in Figure 2. The $Ni(OH)_2$ nanosheets of GN1 are boundary-fuzzy, and their thickness is about 1.75 nm. Also, the number of $Ni(OH)_2$ layers is about 6−7. The nanosheets of GN2 are stacked, and the thickness of one nanosheet is about 9 nm, which is obviously thicker than the nanosheets of GN1, and the number of $Ni(OH)_2$ layers is more than 30.

Figure 3a shows the X-ray diffraction (XRD) patterns of rGO, GN1, GN2, GN5, and pure $Ni(OH)_2$ prepared by the same hydrothermal method. All diffraction peaks have been marked in the patterns, and the result corresponds to the β phase $Ni(OH)_2$ (JCPDS 14-0117). The diffraction peaks of rGO are consistent with the literature, indicating that GO is reduced in the hydrothermal process under alkaline conditions.[32]

https://doi.org/10.1021/acsomega.2c06207
ACS Omega 2023, 8, 6289−6301

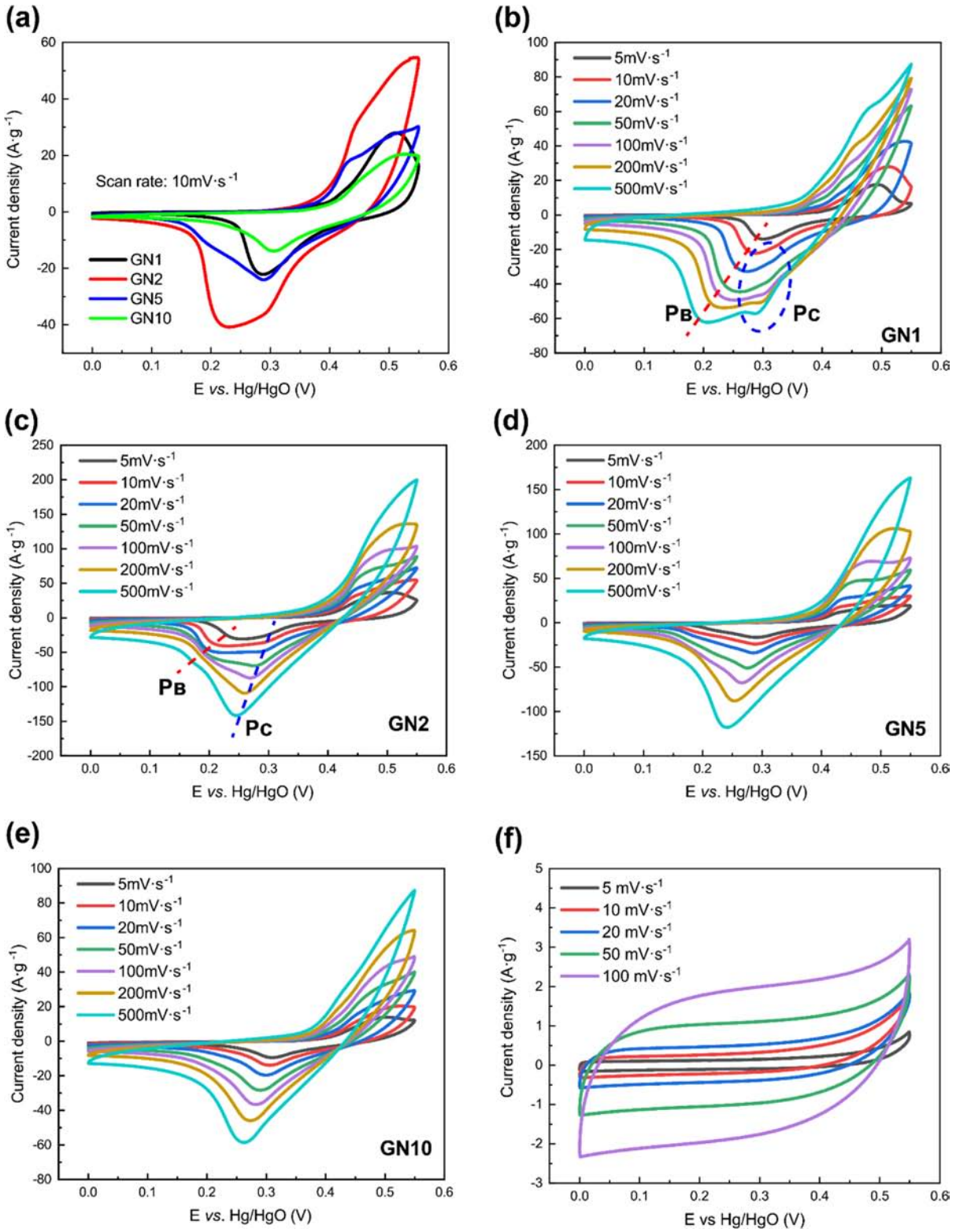

Figure 4. (a) CV curves of GN1, GN2, GN5, and GN10 electrodes at 10 mV s^{-1}. (b–e) CV curves of GN1, GN2, GN5, and GN10 electrodes at different scan rates. (f) CV curves of rGO at different scan rates.

The full-survey-scan X-ray photoelectron spectroscopy (XPS) spectra of GO, GN1, and GN2 are shown in Figure 3b, and the corresponding peak positions have been marked. Ni-related peaks appeared because of the $Ni(OH)_2$ in situ-grown on the surface of GN1 and GN2. The deconvolution result of the GO C 1s spectrum is shown in Figure 3c. The peaks at the binding energies of 284.8, 285.5, and 286.9 eV correspond to C−C, C−O, and C═O functional groups, respectively. This indicates that there are abundant OFGs on the surface of GO, which is an important reason for $Ni(OH)_2$ nanosheets being anchored.[33,34] The inset in Figure 3c shows the Ni 2p spectra of GN1 and GN2. The peaks at 873.7 and

https://doi.org/10.1021/acsomega.2c06207
ACS Omega 2023, 8, 6289−6301

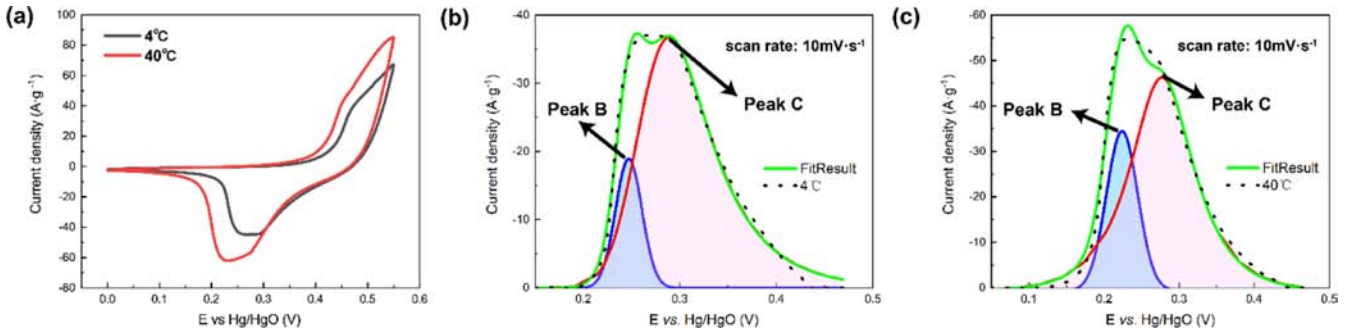

Figure 5. (a) CV curves of GN2 at 4 and 40 °C; CV-peak-differentiation-imitation of GN2 at (b) 4 and (c) 40 °C.

856 eV correspond to Ni $2p_{1/2}$ and Ni $2p_{3/2}$, respectively. The spin energy separation is 17.7 eV, which is in accordance with the fact that $Ni(OH)_2$ is loaded on the rGO surface.[35]

Figure 3d shows the thermogravimetric (TG) curves of GN1, GN2, and GN5. The three curves are similar in shape. The curves are all formed by the thermal weight loss of rGO and $Ni(OH)_2$. The calculation is based on the fact that the final product is NiO, and the final products of GN1, GN2, and GN5 take 57.99, 64.11, and 71.96%, respectively. The mass proportions of $Ni(OH)_2$ in the composite are 71.96, 79.56, and 89.30%, respectively.

The cyclic voltammetry (CV) curves of GN1, GN2, GN5, and GN10 electrodes at 10 mV s^{-1} are shown in Figure 4a. GN2 has the biggest curve area, which corresponds to the maximum specific capacity. The CV curve areas of GN1 and GN5 are close, and the specific capacity of GN10 is the lowest due to the large internal resistance.[36] The specific capacities of GN1, GN2, GN5, and GN10 electrodes are 85.64, 248.34, 143.39, and 80.26 mA h g^{-1}, respectively, calculated from CV curves at 10 mV s^{-1}. Figure 4b–e shows the CV curves of GN1, GN2, GN5, and GN10, respectively, at different scan rates, and the CV specific capacities of them are shown in Figure S5 and Table S1. There is only one reduction peak in the CV curve of GN1 when the scan rate is lower than 20 mV s^{-1}, mainly because of the flat moss-like morphology and the thin $Ni(OH)_2$ layers, and the rGO substrate can export electrons effectively and quickly. As the scan rate increases to 100 mV s^{-1}, the reaction rate is significantly limited by diffusion, and there are two peaks with obvious separation of potential in the high-rate CV curve. One peak at a lower potential (denoted as P_B) gradually shifts to the left, while the position of the other peak at a higher potential (denoted as P_C) hardly changes with the increase in the scan rate. The reduction peak of GN2 shows a platform current response, which can be regarded as a platform peak formed by the coexistence of two peaks, P_B and P_C, respectively. As the scan rate increases, the P_B gradually disappears, while the P_C remains. The peak current of P_C increases significantly, while the left shift of the peak position is ignorable, which conforms to the fast redox response of several $Ni(OH)_2$ layers near the surface less affected by diffusion.[37] The peak current of P_B increases moderately during the scan rate increase. It is worth noting that when the scan rate is higher than 100 mV s^{-1}, the peak gradually passivates and almost disappears at 500 mV s^{-1}. Furthermore, the potential deviation of P_B is nonnegligible at low scan rates, which is consistent with the redox reaction in bulk controlled by diffusion, that is, battery-type behavior. To sum up, there are two behaviors in the negative scanning process of the CV scanning of GN2, a fast response near the surface and a redox reaction in the bulk (battery-type behavior), corresponding to P_C and P_B in the curves, respectively. The morphologies of GN5 and GN10 are different from those of GN1 and GN2, showing nanohexagonal prisms. The near-surface reaction takes a high proportion, and the capacity is mainly contributed by the fast response near the surface, so their CV curves have only one pair of redox peaks. In order to eliminate the influence of rGO on the CV results of the composite electrode, we prepared the electrode containing only rGO. The preparation process is completely consistent with that of the composite electrode. The dosage of NaOH and $NiSO_4{\cdot}6H_2O$ is zero. The CV test results of the corresponding electrodes are shown in Figure 4f. The CV curve of the rGO electrode presents a rectangle, which gradually deforms with the increase of scan rate, without any significant redox peaks. It can be seen from the CV curve of the rGO electrode that its capacity is relatively small, far less than that of several composite electrodes, especially GN2. Therefore, we believe that the redox peaks in the four composite electrodes are not directly provided by rGO.

To prove that the response of the platform peak current formed in the negative scanning of GN2 corresponds to near-surface and bulk redox reactions, respectively, the CV scanning was performed at 4 and 40 °C in Figure 5a. Instantaneous current (j) is based on the following equation during the CV scan

$$j(t) = zFD\frac{C - C(t)}{\delta(t)} \tag{1}$$

The diffusion coefficient (D) follows the Arrhenius equation[38]

$$D = D_0 \exp\left(\frac{E}{RT}\right) \tag{2}$$

The derivative of T over D has

$$\frac{dD}{dT} = -\frac{D_0 E \exp\left(\frac{E}{RT}\right)}{RT^2} \tag{3}$$

where z and F stand for the charge-transfer number of the reaction and Faraday constant, respectively. $D[C - C(t)]/\delta(t)$ stands for the diffusion flux of ions, which has a relationship with the scan rate. E and D_0 are the energy of activation and the pre-exponential factor.[39] It can be seen that when the scan rate is a certain value, the temperature is the only factor affecting the diffusion current. Therefore, the CV scanning with the scan rate of 10 mV s^{-1} at 4 and 40 °C was carried out, and the deconvolution results are shown in Figure 5b,c. Obviously, the proportion of P_C at a lower temperature is

https://doi.org/10.1021/acsomega.2c06207
ACS Omega 2023, 8, 6289−6301

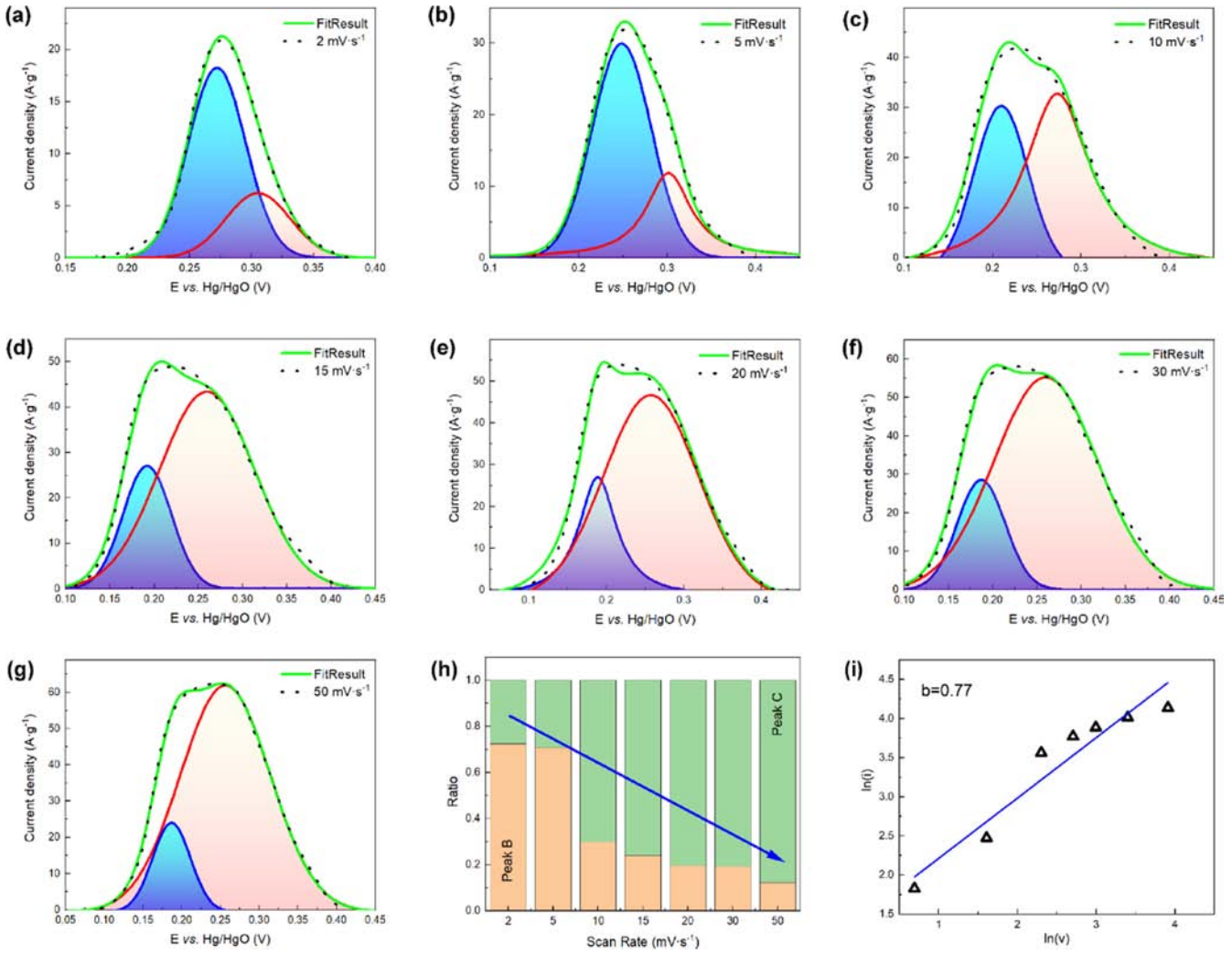

Figure 6. (a–g) CV-peak-differentiation imitation of GN2 at different scan rates; the current density takes the absolute value. (h) Contribution of P_B and P_C. (i) ln of peak current (i) vs ln(v) plot for P_C of GN2.

larger than that at a higher temperature. D_0 can be regarded as a constant in such a temperature range.[39] The E of the near-surface reaction is smaller than that of the bulk redox reaction. After the temperature is elevated to 40 °C, the D and j of the near-surface reaction are smaller than that of the bulk redox reaction, which is in agreement with the experiment result; that is, P_B takes a higher part of the area than P_C at a higher temperature.

In order to prove that the near-surface reaction still exists, the CV curves with the scan rates of 2–50 mV s^{-1} and the deconvolution results are shown in Figure 6a–g. The area integral is calculated from the peak fitting results, as shown in Figure 6h. The proportion of P_C gradually increases with the increase in the scan rate.

Electrochemical energy storage is mainly dominated by the surface-controlled process or the diffusion-controlled process.[40] The current density of CV at low scan rates follows the equation given below.

$$i = av^b \tag{4}$$

The response current and the scan rate are denoted by i and v, and a and b are coefficients. The b value of P_C calculated based on eq 4 is about 0.77. When the value of b is 0.5, the electrochemical behavior is controlled by the diffusion process, and when the value of b is 1, it indicates that the current is dominated by the surface process, which means that the electrochemical behavior is controlled by the capacitive process.[41−43]

Figure 7 shows the XRD patterns obtained by GN2 after CV scanning to 0 and 0.55 V, respectively. In order to eliminate the influence of the conductive additive and current collector, the electrode only uses poly(tetrafluoroethylene) (PTFE) as the binder without a conductive additive and the current collector is marked as GN2FS. In order to avoid electrolyte decomposition and reduce polarization, the CV was scanned at 0.1 mV s^{-1}. Only two diffraction patterns belong to β-$Ni(OH)_2$ (JCPDS 14-0117) and β-NiOOH (JCPDS 06-0141), respectively. Without any diffraction peaks of α (JCPDS 38-0715) and γ (JCPDS 06-0075) phases, indicating that there are not enough α and γ planes exposed. Simultaneously, there are still two significant peaks in the negative CV scan of the electrode with only PTFE and the active material. It shows that the above two peaks have no relationship with the current collector and the conductive additive. Besides, the two peaks are independent of phase transition. If sufficient α and γ phases existed, the intensity of the CV peak resulting from the phase transition should be similar to that of the redox peak, which is contrary to the XRD pattern shown in Figure 7. Therefore, it

https://doi.org/10.1021/acsomega.2c06207
ACS Omega 2023, 8, 6289−6301

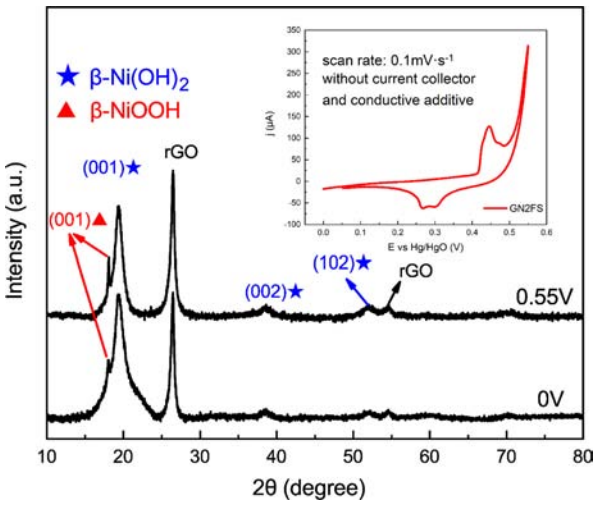

Figure 7. XRD patterns of the GN2 electrode in 0.55 and 0 V during CV scan (inset curve).

can be determined that the bulk and the near-surface reactions are responsible for the formation of the platform's current responses in the CV curves.

Nyquist plots of GN1, GN2, GN5, and GN10 electrodes are shown in Figure 8, and the fitting results are shown in Table 1.

Table 1. Fitting Parameters of GN1, GN2, GN5, and GN10

fitting parameters	GN1	GN2	GN5	GN10
R_s (Ω)	0.68	0.78	0.44	0.39
CPE (Ω)	0.0013	0.0031	0.0106	0.0117
n_{CPE}	0.94	0.97	0.78	0.76
R_{ct} (Ω)	0.45	0.25	2.63	44.29
W (Ω)	2.06	2.03	21.07	236.60
N	0.44	0.41	0.41	0.20

The resistance related to electrolytes and the test system is included in R_s.[44] The R_s of GN1, GN2, GN5, and GN10 electrodes are close, meaning that a stable test system was employed in the electrochemical impedance spectroscopy (EIS) test. The CPE resistance of GN1, GN2, GN5, and GN10 electrodes increased with the increase of nickel source dosage. The n_{CPE} of GN1 and GN2 electrodes are closer to 1, which means that their electrochemical behavior is closer to that of capacitance. The main reason is that the moss-like morphology of GN1 and GN2 exposed more redox reaction sites than GN5 and GN10; meanwhile, the existence of rGO can help with electron conduction. R_{ct} is the charge-transfer resistance and has a relationship with the redox reaction.[45,46] The R_{ct} value of GN2, which has more nickel source dosage than GN1, is smaller, which is mainly due to the higher reduction degree of rGO caused by more dosage of NaOH. The higher reduced

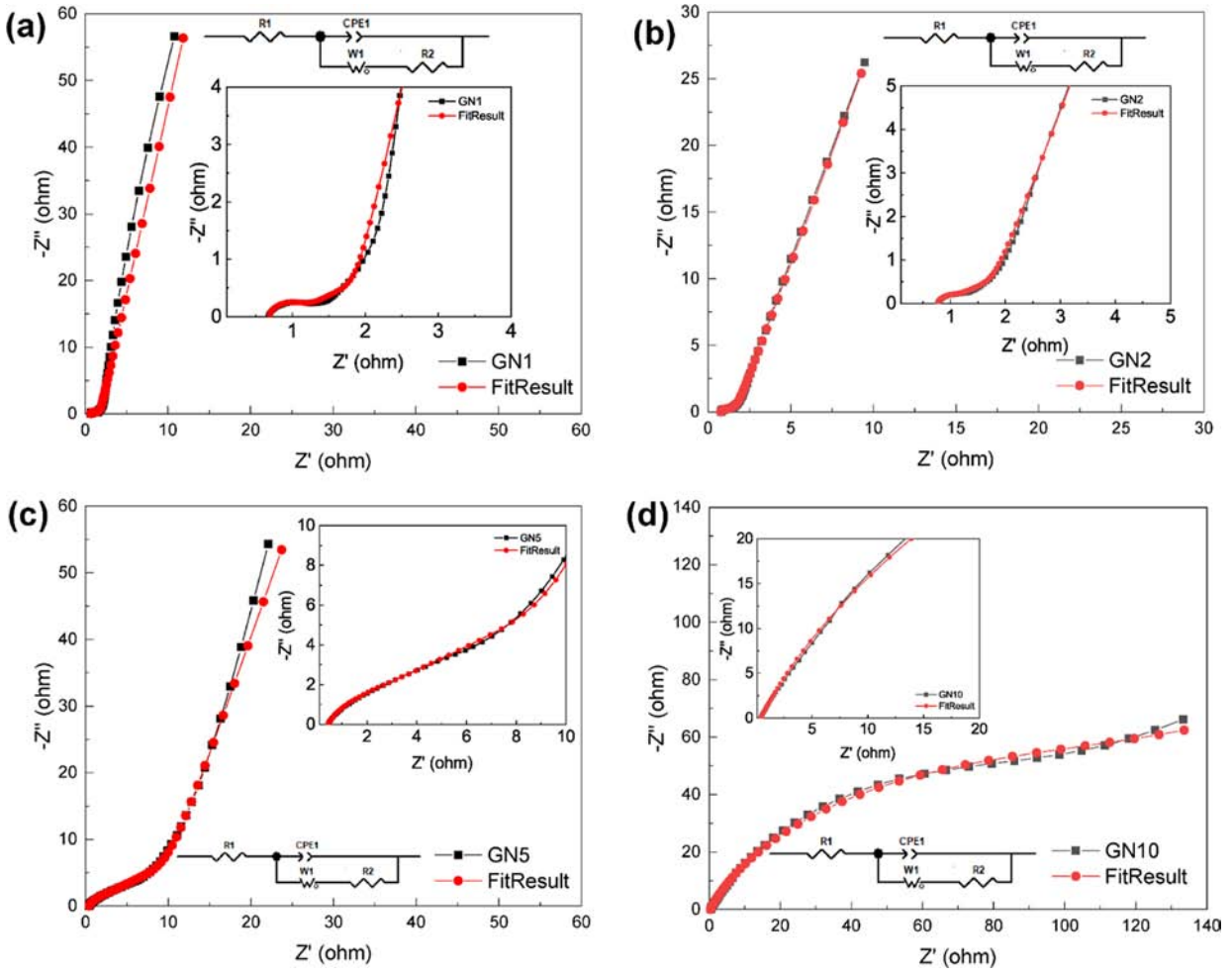

Figure 8. Nyquist plots with fitting data of (a) GN1, (b) GN2, (c) GN5, and (d) GN10 at OCP, and the inset is the related equivalent circuit.

https://doi.org/10.1021/acsomega.2c06207
ACS Omega 2023, 8, 6289−6301

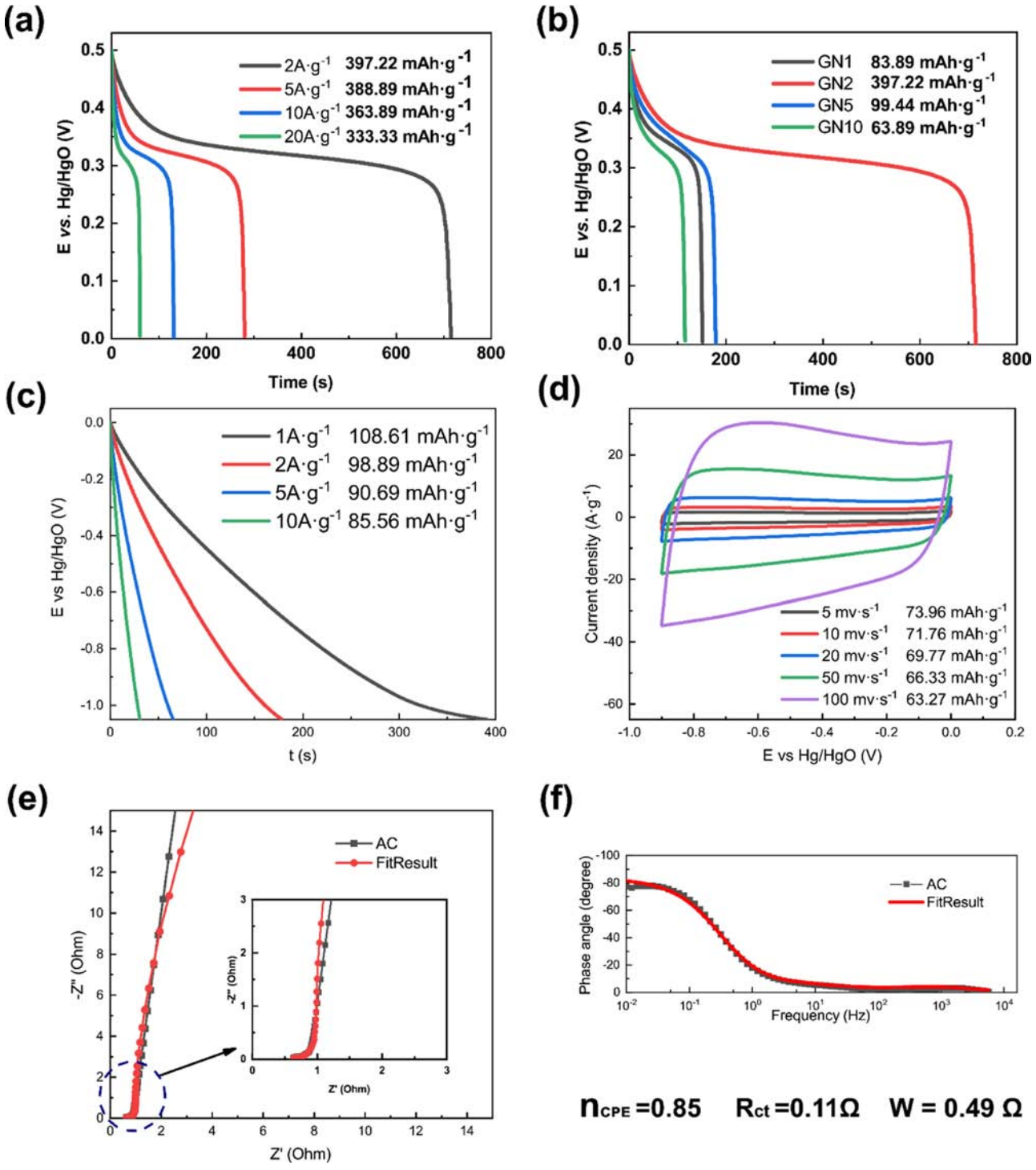

Figure 9. (a) GD curves of GN2 at different current densities. (b) GD curves of GN1, GN2, GN5, and GN10 at 2 A g^{-1}. (c) GD curves of GN2 at different current densities. (d) CV curves of AC at different scan rates. (e) Nyquist plots with fitting data of AC at OCP. (f) Bode plots with fitting data of AC at OCP.

degree of rGO can provide better conductivity which causes an easier redox reaction. Due to the obvious change in the particle morphology and the increased thickness of GN5 and GN10, the proton diffusion speed decreases, resulting in a significant increase in the Walburg impedance of GN5 and GN10, which represents the diffusion process impedance.

The galvanostatic discharge (GD) curves of GN2 at 2, 5, 10, and 20 A g^{-1} are shown in Figure 9a, and the specific capacities marked in are 397.22, 388.89, 363.89, and 333.33 mA h g^{-1}, respectively. The retention rate is as high as 84% during the current density enlarged from 2 to 20 A g^{-1}. The GD curves of GN1, GN2, GN5, and GN10 electrodes at 2 A g^{-1} are shown in Figure 9b, and the marked specific capacities are 83.89, 397.22, 99.44, and 63.89 mA h g^{-1}, respectively. The moss-like morphology causes a large number of redox-active sites at the electrode/electrolyte interface, and the conductive network formed by rGO can ensure the rapid transmission of electrons

https://doi.org/10.1021/acsomega.2c06207
ACS Omega 2023, 8, 6289−6301

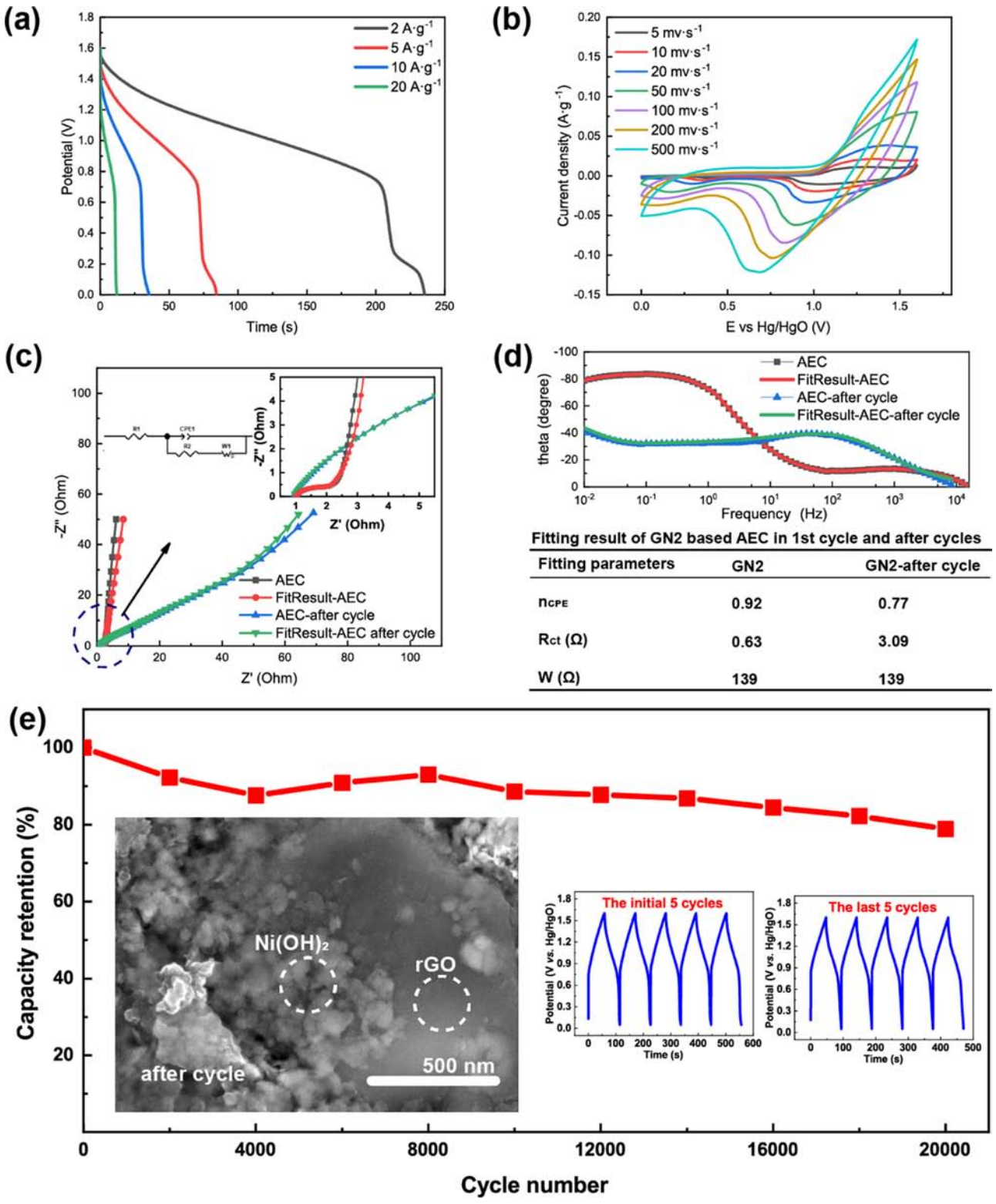

Fitting result of GN2 based AEC in 1st cycle and after cycles

Fitting parameters	GN2	GN2-after cycle
n_{CPE}	0.92	0.77
R_{ct} (Ω)	0.63	3.09
W (Ω)	139	139

Figure 10. (a) GD curves of GN2-based AEC at different current densities. (b) CV curves of GN2-based AEC at different scan rates. (c) Nyquist plots with fitting data of GN2-based AEC at OCP. (d) Bode plots with fitting data of GN2-based AEC at OCP. (e) Stability of the AEC. Insets are the SEM image of the GN2 electrode after cycles; initial and last five cycles of the AEC.

and protons, resulting in lower internal resistance and outstanding performance of GN2.

GD, CV, and EIS measurements of AC were carried out to investigate the electrochemical performance in Figure 9c–f. GD was performed at different current densities ranging from 1 to 10 A g^{-1} in Figure 9c, and the linear discharge profile reflected the electrochemical double layer (EDLC) behavior of the material. The material retained almost 78.78% of its specific capacity (108.61 mA h g^{-1} at 1 A g^{-1}; 85.56 mA h g^{-1} at 10 A g^{-1}), evidencing high electronic conductivity.

https://doi.org/10.1021/acsomega.2c06207
ACS Omega 2023, 8, 6289−6301

The CV curves were performed at different scan rates, Figure 9d, evidencing a rectangular feature resulting from the electric double-layer charge storage mechanism characteristic of AC. The redox current response increases continuously with increasing scan rate which evidences the highly reversible EDLC processes at the electrode/electrolyte interface.

The EIS spectra at OCP and the equivalent circuit used to fit the data are illustrated in Figure 9e, and the fitting parameters are marked in Figure 9f. The absence of a semicircle in the high-frequency region can be noticed from the magnified plot shown in the inset of Figure 9e, and the resistance value of only 0.11 Ω suggests negligible charge-transfer resistance, as expected for highly conductive materials.[46] It is worth pointing out that the Warburg resistance value is tiny at about 0.49 Ω. The small charge-transfer resistance and the decreased diffusion effect can explain the fast reversible processes at the carbon/electrolyte interface. In the low-frequency region (1−0.01 Hz), the presence of a nearly vertical line and phase-angle values approaching −80° (can be seen from the Bode plot in Figure 9f) with a n_{CPE} value of 0.85 indicates an almost ideal capacitive response.[47]

The AC negative electrode and GN2 are used to assemble an AEC for the cycling test at 2, 5, 10, and 20 A g^{-1}, and the results are shown in Figure 10a. The mass balancing details of the AEC are exhibited in the Supporting Information. After calculation, the AEC obtained a 36.34 W h kg^{-1} energy density at a 555.98 W kg^{-1} power density and a 16.16 W h kg^{-1} energy density at a 4843.85 W kg^{-1} power density; the detailed data are shown in Table 2.

Table 2. Energy Density and Power Density of GN2-Based AEC

current density (A g^{-1})	energy density (W h kg^{-1})	power density (W kg^{-1})
2	36.34	555.98
5	30.91	1319.86
10	24.68	2513.62
20	16.16	4843.85

The CV curves of AEC at 10−500 mV s^{-1} are shown in Figure 10b, which show a clear and full redox peak of the CV curve at a low scan rate, which proves that the electrode reaction is adequate.

The Nyquist plots with a Bode plot of the AEC and after the cycle are shown in Figure 10c,d, and the fitting results are shown in Figure 10d. After cyclic stabilization of AEC, the morphology of $Ni(OH)_2$ nanosheets changed, and the proportion of the diffusion behavior increased, which led to the decrease of n_{CPE} of GN2-based AEC. The R_{ct} value of AEC after the cycle is 3.09 Ω higher than that of the initial cycle, caused by the low conductivity of the electrode after the cycle. The high Warburg impedance of AEC after the cycle confirms that the impedance controlled by the diffusion process increases. In the low-frequency region (1−0.01 Hz), the presence of a line and phase angle values approaching −40° (can be seen from the Bode plot in Figure 10d) with the n_{CPE} exponent (n) value of 0.77 indicates AEC after the cycle had low conductivity and high polarization.

As shown in Figure 10e, after 20,000 cycles, the capacity retention rate is as high as 79%. Due to the maintenance of battery-type behavior, the device had a considerable energy density. Simultaneously, the redox-active sites provided by the moss-like morphology and the high conductivity of rGO make the device stable during the cycles.

The SEM image of the GN2 electrode after the cycle is provided in the insert of Figure 10e. The SEM picture is relatively blurred due to the addition of PTFE. Due to the charge−discharge cycle, the $Ni(OH)_2$ nanosheets are passivated at the edge and agglomerated. Therefore, the AEC capacity is reduced compared to the initial cycles.

CONCLUSIONS

Herein, we use a simple hydrothermal method to synthesize a $Ni(OH)_2$−rGO composite and control the size and the number of lattice layers of $Ni(OH)_2$ nanosheets which were grown on a rGO substrate by changing the dosage of the nickel source material. The $Ni(OH)_2$−rGO composite with a moss-like morphology which is named GN2 was prepared to ensure that it retained the battery-type behavior in the electrochemical process so as to obtain a high-capacity electrode. The OFG on the rGO surface can anchor $Ni(OH)_2$ particles to prevent their aggregation. The rGO substrate after hydrothermal reduction can rapidly export ions and electrons, significantly reducing a series of problems caused by the size of $Ni(OH)_2$ nanosheets. The electrode has a specific capacity of 397.22 mA h g^{-1} at 2 A g^{-1}, and the retention rate is 84% with the current density rising to 20 A g^{-1}. Using AC as a negative electrode to prepare an AEC that has a 30.91 W h kg^{-1} energy density at 1319.86 W kg^{-1}, the retention rate can reach 79% after 20,000 cycles. The nanocrystallization of battery-type materials is effective in solving problems such as large internal resistance and easy degradation in the process of charging and discharging. However, excessive nanocrystallization will lead to surface layer effects which will greatly reduce the capacity of materials. Therefore, an appropriate particle size of about 50 nm, the number of lattice layers of more than 30, and the micromorphology of nanosize battery-type material should be explored to ensure that the materials can store energy mainly by the battery-type behavior. Meanwhile, the conductive network is constructed to assist the export of electrons and ions, reduce internal resistance, and prevent the material from aggregating. The electrode with high-rate capability and long cycle performance can be obtained, and it can retain the large capacity of the battery-type material concurrently. While retaining many advantages of electrochemical capacitors, this research effectively makes up for the lack of energy density, which provides a new idea for follow-up research.

EXPERIMENTAL SECTION

Synthesis of the $Ni(OH)_2$−rGO Composite. $Ni(OH)_2$−rGO composites were prepared by the hydrothermal method using $NiSO_4{\cdot}6H_2O$, NaOH, and GO as raw materials. By changing the dosage of $NiSO_4{\cdot}6H_2O$ and NaOH, the mass ratios of GO and $Ni(OH)_2$ were 1:1, 1:2, 1:5, and 1:10, which were named GN1, GN2, GN5, and GN10, respectively. Meanwhile, pure $Ni(OH)_2$ powder and pure rGO were prepared by the same method as the controls.

Characterization Methods. The morphology of the prepared samples was analyzed by SEM (SU8100, HITACHI) and TEM (F20, FEI). AFM (BRUKER ICON) was used to measure the thickness of nanosheets. Phase analysis and crystal structure characterization were performed using XRD (D8 Focus, Bruker). XPS was performed using an ESCALAB 250Xi

https://doi.org/10.1021/acsomega.2c06207
ACS Omega 2023, 8, 6289−6301

system (Thermo Fisher). TG curves were measured by STA 449C (NETZSCH) in the air at a heating rate of 10 K min^{-1}.

Electrode Fabrication. The $Ni(OH)_2$−rGO composite, PTFE, and acetylene black were mixed to prepare electrode slurry in a ratio of 8:1:1 and were uniformly dispersed on the nickel foam collector. Finally, the $Ni(OH)_2$−rGO composite electrode was fabricated by pressing and vacuum drying.

Electrochemical Measurements. Electrochemical measurements, such as CV tests, EIS, and GD tests, were performed in a three-electrode half-cell using an electrochemical workstation (CHI660E, Chenhua), with a Pt electrode as the counter electrode and Hg/HgO as the reference electrode. The stability of the AEC was performed using a battery testing system (M340A, LANHE).

The details of the material synthesis method, electrochemical measurement, and data calculation are described in the Supporting Information.

■ ASSOCIATED CONTENT

Supporting Information

The Supporting Information is available free of charge at https://pubs.acs.org/doi/10.1021/acsomega.2c06207.

Particle size distribution of GN2 and GN5; interplanar distance of GN2; SEM images of GN1, GN2, and GN5; SEM images of GN10, $Ni(OH)_2$, and rGO at different magnifications; comparison of CV specific capacities of the samples at different scan rates; CV specific capacities of the samples at different scan rates; GD specific capacities of GN2 at various current densities; GD specific capacities of GN1, GN2, GN5, and GN10 at 2 A g^{-1}; and experimental details (PDF)

■ AUTHOR INFORMATION

Corresponding Author

Meicheng Li − *State Key Laboratory of Alternate Electrical Power System with Renewable Energy Sources, School of New Energy, North China Electric Power University, Beijing 102206, China*; orcid.org/0000-0002-0731-741X; Email: mcli@ncepu.edu.cn

Authors

Binglin Guo − *State Key Laboratory of Alternate Electrical Power System with Renewable Energy Sources, School of New Energy, North China Electric Power University, Beijing 102206, China*

Yihao Gao − *State Key Laboratory of Alternate Electrical Power System with Renewable Energy Sources, School of New Energy, North China Electric Power University, Beijing 102206, China*

Yongyue Li − *State Key Laboratory of Alternate Electrical Power System with Renewable Energy Sources, School of New Energy, North China Electric Power University, Beijing 102206, China*

Kai Liu − *State Key Laboratory of Alternate Electrical Power System with Renewable Energy Sources, School of New Energy, North China Electric Power University, Beijing 102206, China*

Xiaojun Lv − *State Key Laboratory of Alternate Electrical Power System with Renewable Energy Sources, School of New Energy, North China Electric Power University, Beijing 102206, China*

Changhua Mi − *State Key Laboratory of Alternate Electrical Power System with Renewable Energy Sources, School of New Energy, North China Electric Power University, Beijing 102206, China*

Lehao Liu − *State Key Laboratory of Alternate Electrical Power System with Renewable Energy Sources, School of New Energy, North China Electric Power University, Beijing 102206, China*

Complete contact information is available at: https://pubs.acs.org/10.1021/acsomega.2c06207

Notes

The authors declare no competing financial interest.

■ ACKNOWLEDGMENTS

This work was supported partially by the project of the State Key Laboratory of Alternate Electrical Power System with Renewable Energy Sources (LAPS21004 and LAPS202114), Hebei Natural Science Foundation (E2022502022), National Natural Science Foundation of China (grant nos. 52272200, 51972110, 52102245, and 52072121), Beijing Science and Technology Project (Z211100004621010), Beijing Natural Science Foundation (2222076 and 2222077), Huaneng Group Headquarters Science and Technology Project (HNKJ20-H88), 2022 Strategic Research Key Project of Science and Technology Commission of the Ministry of Education, the Fundamental Research Funds for the Central Universities (2022MS030, 2021MS028, 2020MS023, and 2020MS028), and the NCEPU "Double First-Class" Program.

■ REFERENCES

(1) Natarajan, S.; Ulaganathan, M.; Aravindan, V. Building next-generation supercapacitors with battery type $Ni(OH)_2$. *J. Mater. Chem. A* **2021**, *9*, 15542−15585.

(2) Schmuch, R.; Wagner, R.; Hörpel, G.; Placke, T.; Winter, M. Performance and Cost of Materials for Lithium-Based Rechargeable Automotive Batteries. *Nat. Energy* **2018**, *3*, 267−278.

(3) Dunn, B.; Kamath, H.; Tarascon, J. M. Electrical Energy Storage for the Grid: A Battery of Choices. *Science* **2011**, *334*, 928−935.

(4) Shen, F. Y.; Dixit, M. B.; Xiao, X. H.; Hatzell, K. B. Effect of Pore Connectivity on Li Dendrite Propagation within LLZO Electrolytes Observed with Synchrotron X-ray Tomography. *ACS Energy Lett.* **2018**, *3*, 1056−1061.

(5) Kumar, S.; Saeed, G.; Zhu, L.; Hui, K. N.; Kim, N. H.; Lee, J. H. 0D to 3D carbon-based networks combined with pseudocapacitive electrode material for high energy density supercapacitor: A review. *Chem. Eng. J.* **2021**, *403*, 126352.

(6) Xu, X. B.; Li, S. H.; Zhang, H.; Shen, Y.; Zakeeruddin, S. M.; Graetzel, M.; Cheng, Y. B.; Wang, M. K. A Power Pack Based on Organometallic Perovskite Solar Cell and Supercapacitor. *ACS Nano* **2015**, *9*, 1782−1787.

(7) Yang, Z.; Tian, J.; Yin, Z.; Cui, C.; Qian, W.; Wei, F. Carbon nanotube- and graphene-based nanomaterials and applications in high-voltage supercapacitor: A review. *Carbon* **2019**, *141*, 467−480.

(8) Liang, J.; Qu, T.; Kun, X.; Zhang, Y.; Chen, S.; Cao, Y.-C.; Xie, M.; Guo, X. Microwave Assisted Synthesis of Camellia Oleifera Shell-Derived Porous Carbon with Rich Oxygen Functionalities and Superior Supercapacitor Performance. *Appl. Surf. Sci.* **2018**, *436*, 934−940.

(9) Wang, Q.; Zhang, Z. J.; Shen, F.; Zhao, B.; Han, X. G. Holey graphene oxide as filler to improve electrochemical performance of solid polymer electrolytes. *Mater. Express* **2019**, *9*, 1055−1061.

(10) You, H. J.; Xuan, Y. Y.; Zuo, Y.; Shen, F.; Han, X. G.; Fang, J. X. Insight of holey-graphene in the enhancing of electrocatalytic activity as supporting material. *Nanotechnology* **2018**, *29*, 425708.

(11) Korkmaz, S.; Kariper, İ. A.; Karaman, O.; Karaman, C. The production of rGO/ RuO_2 aerogel supercapacitor and analysis of its electrochemical performances. *Ceram. Int.* **2021**, *47*, 34514−34520.
(12) Ryu, I.; Kim, D.; Choe, G.; Jin, S.; Hong, D. J.; Yim, S. Monodisperse RuO_2 nanoparticles for highly transparent and rapidly responsive supercapacitor electrodes. *J. Mater. Chem. A* **2021**, *9*, 26172−26180.
(13) Wan, J.; Ji, P. Y.; Li, B. X.; Xi, Y.; Gu, X.; Huang, L.; He, M. Q.; Hu, C. G. Enhanced Electrochemical Performance in an Aluminium Doped δ-MnO_2 Supercapacitor Cathode: Experimental and Theoretical Investigations. *Chem. Commun.* **2022**, *58*, 589−592.
(14) Jeong, J. H.; Kim, Y. A.; Kim, B.-H. Electrospun Polyacrylonitrile/Cyclodextrin-Derived Hierarchical Porous Carbon Nanofiber/MnO_2 Composites for Supercapacitor Applications. *Carbon* **2020**, *164*, 296−304.
(15) Ma, Y.; Sheng, H.; Dou, W.; Su, Q.; Zhou, J.; Xie, E.; Lan, W. Fe_2O_3 Nanoparticles Anchored on the $Ti_3C_2T_x$ MXene Paper for Flexible Supercapacitors with Ultrahigh Volumetric Capacitance. *ACS Appl. Mater. Interfaces* **2020**, *12*, 41410−41418.
(16) Nguyen, V. T.; Ting, J.-M. A Redox-Additive Electrolyte and Nanostructured Electrode for Enhanced Supercapacitor Energy Density. *ACS Sustainable Chem. Eng.* **2020**, *8*, 18023−18033.
(17) Gogotsi, Y.; Penner, R. M. Energy Storage in Nanomaterials-Capacitive Pseudocapacitive, or Battery-like? *ACS Nano* **2018**, *12*, 2081−2083.
(18) Jiang, Y. Q.; Liu, J. P. Definitions of Pseudocapacitive Materials: A Brief Review. *Energy Environ. Mater.* **2019**, *2*, 30−37.
(19) Sharma, G. P.; Vikas, R. G.; Pala, S.; Sivakumar, S. Size induced Extrinsic Pseudocapacitance in Ultrasmall $CoMoO_4$ Nanocluster. *Energy Fuels* **2021**, *35*, 19765−19774.
(20) Xie, M.; Duan, S.; Shen, Y.; Fang, K.; Wang, Y.; Lin, M.; Guo, X. In-Situ-Grown $Mg(OH)_2$-Derived Hybrid α-$Ni(OH)_2$ for Highly Stable Supercapacitor. *ACS Energy Lett.* **2016**, *1*, 814−819.
(21) Li, W. Y.; Zhang, B. J.; Lin, R. J.; Ho-Kimura, S.; He, G. J.; Zhou, X. Y.; Hu, J. Q.; Parkin, I. P. A Dendritic Nickel Cobalt Sulfide Nanostructure for Alkaline Battery Electrodes. *Adv. Funct. Mater.* **2018**, *28*, 1705937.
(22) Yi, H.; Wang, H.; Jing, Y.; Peng, T.; Wang, Y.; Guo, J.; He, Q.; Guo, Z.; Wang, X. Advanced Asymmetric Supercapacitors Based on CNT@$Ni(OH)_2$ Core-Shell Composites and 3D Graphene Networks. *J. Mater. Chem. A* **2015**, *3*, 19545−19555.
(23) Zhang, J. T.; Liu, S.; Pan, G. L.; Li, G. R.; Gao, X. P. A 3D hierarchical porous α-$Ni(OH)_2$/graphite nanosheet composite as an electrode material for supercapacitors. *J. Mater. Chem. A* **2014**, *2*, 1524−1529.
(24) Luo, X.; Shao, J.; He, P.; Zhong, M.; Wang, Q.; Li, K.; Zhao, W. Metal organic framework derived CoS_2@$Ni(OH)_2$ core-shell structure nanotube arrays for high-performance flexible hybrid supercapacitors. *Electrochim. Acta* **2020**, *354*, 136679.
(25) Li, S.; Sharma, N.; Yu, C.; Zhang, Y.; Wan, G.; Fu, R.; Huang, H.; Sun, X.; Lee, S.-J.; Lee, J.-S.; Nordlund, D.; Pianetta, P.; Zhao, K.; Liu, Y.; Qiu, J. Operando Tailoring of Defects and Strains in Corrugated beta-Ni(OH)2 Nanosheets for Stable and High-Rate Energy Storage. *Adv. Mater.* **2021**, *33*, 2006147.
(26) Li, W.; Huang, Z.; Jia, Y.; Cui, Y.; Shi, P.; Li, T.; Yue, H.; Wang, J.; He, W.; Lou, X. Sulfate assisted synthesis of α-type nickel hydroxide nanowires with 3D reticulation for energy storage in hybrid supercapacitors. *Mater. Chem. Front.* **2022**, *6*, 94−102.
(27) Gibot, P.; Casas-Cabanas, M.; Laffont, L.; Levasseur, S.; Carlach, P.; Hamelet, S.; Tarascon, J. M.; Masquelier, C. Room-Temperature Single-Phase Li Insertion/Extraction in Nanoscale $Li_{(x)}FePO_4$. *Nat. Mater.* **2008**, *7*, 741−747.
(28) Malik, R.; Burch, D.; Bazant, M.; Ceder, G. Particle size dependence of the ionic diffusivity. *Nano Lett.* **2010**, *10*, 4123−4127.
(29) Gaberscek, M.; Dominko, R.; Jamnik, J. Is small particle size more important than carbon coating? An example study on $LiFePO_4$ cathodes. *Electrochem. Commun.* **2007**, *9*, 2778−2783.
(30) Okubo, M.; Hosono, E.; Kim, J.-D.; Enomoto, M.; Kojima, N.; Kudo, T.; Zhou, H.; Honma, I. Nanosize Effect on High-Rate Li-Ion Intercalation in $LiCoO_2$ Electrode. *J. Am. Chem. Soc.* **2007**, *129*, 7444−7452.
(31) Li, J.; Cao, W.; Zhou, N.; Xu, F.; Chen, N.; Liu, Y.; Du, G. Hierarchically Nanostructured $Ni(OH)_2$−MnO_2@C Ternary Composites Derived from Ni-MOFs Grown on Nickel Foam as High-Performance Integrated Electrodes for Hybrid Supercapacitors. *Electrochim. Acta* **2020**, *343*, 136139.
(32) Zhu, J. W.; Chen, S.; Zhou, H.; Wang, X. Fabrication of a Low Defect Density Graphene-Nickel Hydroxide Nanosheet Hybrid with Enhanced Eectrochemical Performance. *Nano Res.* **2012**, *5*, 11−19.
(33) Tian, J.; Shan, Q.; Yin, X.; Wu, W. A Facile Preparation of Graphene/Reduced Graphene Oxide/$Ni(OH)_2$ Two Dimension Nanocomposites for High Performance Supercapacitors. *Adv. Powder Technol.* **2019**, *30*, 3118−3126.
(34) Mkhoyan, K. A.; Contryman, A. W.; Silcox, J.; Stewart, D. A.; Eda, G.; Mattevi, C.; Miller, S.; Chhowalla, M. Atomic and Electronic Structure of Graphene-Oxide. *Nano Lett.* **2009**, *9*, 1058−1063.
(35) Wang, K.; Zhang, X.; Zhang, X.; Chen, D.; Lin, Q. A Novel $Ni(OH)_2$/Graphene Nanosheets Electrode with High Capacitance and Excellent Cycling Stability for Pseudocapacitors. *J. Power Sources* **2016**, *333*, 156−163.
(36) Chakrabarty, N.; Chakraborty, A. K. Controlling the Electrochemical Performance of β-$Ni(OH)_2$/Carbon Nanotube Hybrid Electrodes for Supercapacitor Applications by La Doping: A Systematic Investigation. *Electrochim. Acta* **2019**, *297*, 173−187.
(37) Conway, B. E. Transition from "Supercapacitor" to "Battery" Behavior in Electrochemical Energy Storage. *J. Electrochem. Soc.* **1991**, *138*, 1539.
(38) Dick, K.; Dhanasekaran, T.; Zhang, Z.; Meisel, D. Size-Dependent Melting of Silica-Encapsulated Gold Nanoparticles. *J. Am. Chem. Soc.* **2002**, *124*, 2312−2317.
(39) Rees, L.; Rao, A. Self-Diffusion of Various Cations in Natural Mordenite. *Trans. Faraday Soc.* **1966**, *62*, 2103−2110.
(40) Lindström, H.; Södergren, S.; Solbrand, A.; Rensmo, H.; Hjelm, J.; Anders, H.; Lindquist, S.-E. Li^+ Ion Insertion in TiO_2 (Anatase). 2. Voltammetry on Nanoporous Films. *J. Phys. Chem. B* **1997**, *101*, 7717−7722.
(41) Sathiya, M.; Prakash, A. S.; Ramesha, K.; Tarascon, J. M.; Shukla, A. K. V_2O_5-Anchored Carbon Nanotubes for Enhanced Electrochemical Energy Storage. *J. Am. Chem. Soc.* **2011**, *133*, 16291−16299.
(42) Lai, L.; Clark, M.; Su, S.; Li, R.; Ivey, D. G.; Zhu, X. Dip-Coating Synthesis of rGO/α-$Ni(OH)_2$@Nickel Foam with Layer-by-Layer Structure for High Performance Binder-Free Supercapacitors. *Electrochim. Acta* **2021**, *368*, 137589.
(43) Zhang, W.; Wu, Y.; Xu, Z.; Li, H.; Xu, M.; Li, J.; Dai, Y.; Zong, W.; Chen, R.; He, L.; Zhang, Z.; Brett, D. J. L.; He, G.; Lai, Y.; Parkin, I. P. Rationally Designed Sodium Chromium Vanadium Phosphate Cathodes with Multi-Electron Reaction for Fast-Charging Sodium-Ion Batteries. *Adv. Energy Mater.* **2022**, *12*, 2201065.
(44) He, Z.; Mansfeld, F. Exploring the Use of Electrochemical Impedance Spectroscopy (EIS) in Microbial Fuel Cell Studies. *Energy Environ. Sci.* **2009**, *2*, 215−219.
(45) Kim, B. K.; Chabot, V.; Yu, A. P. Carbon Nanomaterials Supported $Ni(OH)_2$/NiO Hybrid Flower Structure for Supercapacitor. *Electrochim. Acta* **2013**, *109*, 370−380.
(46) Chen, R.; Ling, H.; Huang, Q.; Yang, Y.; Wang, X. Interface Engineering on Cellulose-Based Flexible Electrode Enables High Mass Loading Wearable Supercapacitor with Ultrahigh Capacitance and Energy Density. *Small* **2022**, *18*, No. e2106356.
(47) Upadhyay, K. K.; Bundaleska, N.; Abrashev, M.; Bundaleski, N.; Teodoro, O. M. N. D.; Fonseca, I.; de Ferro, A. M.; Tatarova, R. P.; Montemor, E.; Montemor, M. F. Free-standing N-Graphene as conductive matrix for $Ni(OH)_2$ based supercapacitive electrodes. *Electrochim. Acta* **2020**, *334*, 135592.

https://doi.org/10.1021/acsomega.2c06207
ACS Omega 2023, 8, 6289−6301